

IndIGO-D: Probing Compact Binary Coalescences in the Decihertz GW Band

Abhishek Sharma^{1,*} Divya Tahelyani^{1,†} Anand S. Sengupta^{1,‡} and Sanjit Mitra^{2,§}

¹*Department of Physics, Indian Institute of Technology Gandhinagar, Gujarat 382055, India.*

²*Inter-University Centre for Astronomy and Astrophysics (IUCAA), Pune 411007, India*

We study IndIGO-D, a decihertz gravitational-wave mission concept, focusing on a specific configuration in which three spacecraft fly in formation to form an L-shaped interferometer in a heliocentric orbit. The two orthogonal arms share a common vertex, providing a space-based analogue of terrestrial Michelson detectors, while operating in an optimised configuration that yields ppm-level arm-length stability. Assuming 1000 km arm lengths, we analyse the orbital motion and antenna response, and assess sensitivity across the 0.1 – 10 Hz band bridging LISA and next-generation ground-based interferometers. Using fiducial sensitivity curves provided by the IndIGO-D collaboration, we compute horizon distances for different source classes. Intermediate-mass black-hole binaries with masses 10^2 – $10^3 M_\odot$ are detectable to redshifts $z \sim 10^3$, complementing the reach of LISA and terrestrial detectors. Binary neutron star systems are observable to a horizon distance of $z \lesssim 0.3$, allowing continuous multi-band coverage with Voyager-class interferometers from the decihertz regime to merger. A Bayesian parameter-estimation study of a GW170817-like binary shows that the sky localization area improves from $\sim 21 \text{ deg}^2$ at one month to 0.3 deg^2 at six hours pre-merger! These sky areas are readily tiled by wide-field time-domain telescopes such as the Rubin Observatory, whose 9.6 deg^2 field of view and r-band depth enable high-cadence, repeated coverage of GW170817-like kilonovae at this distance and beyond. IndIGO-D exploits the rapid evolution of binaries in the decihertz band to bridge the gap between millihertz and terrestrial observations, enabling early warnings on timescales from months to hours and enhancing the prospects for multi-band and multi-messenger discoveries.

I. INTRODUCTION

The field of gravitational-wave (GW) astronomy has undergone a remarkable transformation since the first direct detection of astrophysical GW signals by the twin Laser Interferometer GW Observatories (LIGO) in 2015 [1, 2]. Over the course of its successive observing runs, the global network of ground-based detectors comprising the LIGO observatories in the United States, Virgo in Italy, and KAGRA in Japan have detected ~ 300 compact binary mergers, uncovering a diverse population, including binary black holes (BBHs), binary neutron stars (BNSs), and potential neutron star black hole (NSBH) systems [3–8]. These discoveries have not only confirmed the existence of stellar-mass black hole binaries but also opened new avenues for astrophysics, cosmology, and fundamental physics. For instance, the detection of GW170817 [9] and its associated electromagnetic counterparts [10] inaugurated the era of multi-messenger astronomy with GWs, allowing for

independent measurements of the Hubble constant [11], insights into the origin of heavy elements [12], and tests of the speed of gravity [13]. The recent fourth observing run (O4) continues to enrich this catalog, enhancing our understanding of binary population properties [14], black hole spins, and tests of general relativity.

Despite these achievements, ground-based detectors such as LIGO are fundamentally limited in sensitivity at low frequencies ($\lesssim 10$ Hz) due to seismic, Newtonian, and suspension thermal noise [15]. As a result, they primarily observe the late inspiral, merger, and ringdown phases of compact binaries, typically lasting from a few seconds to less than a minute in-band. Extending GW observations to lower frequencies can unlock longer-duration signals, enabling us to study earlier inspiral phases with exquisite precision. The deci-Hertz (dHz; ~ 0.1 – 10 Hz) frequency band occupies a crucial observational gap between the milli-Hertz (mHz) regime targeted by space-based detectors like the Laser Interferometer Space Antenna (LISA) [16] and the hecto to kHz range of ground-based interferometers. This intermediate frequency band hosts a rich variety of astrophysical sources, including the inspiral stages of stellar-mass compact binaries that eventually merge in the LIGO band, binaries involving intermediate-mass black holes (IMBHs), and potentially new classes of exotic sources.

* sharma.abhishek@iitgn.ac.in

† divya.tahelyani@iitgn.ac.in

‡ asengupta@iitgn.ac.in

§ sanjit@iucaa.in

A detector sensitive in the dHz regime offers unique scientific advantages. Refs. [17–19] highlight several fundamental questions that remain beyond the reach of both ground-based detectors and space-based observatories sensitive in the mHz band, yet could be effectively addressed by detectors in the dHz frequency range. These include uncovering the progenitors of Type Ia supernovae, probing dynamical signatures of the environments in which compact binaries merge, exploring the population and growth of intermediate-mass black holes, tracing the evolutionary pathways of stellar-mass compact objects, and investigating the formation of the light-seed black holes that may grow into the massive black holes observed at galactic centers.

In addition to addressing these questions, observations in the dHz band will capture a much longer stretch of the inspiral phase of the signal from stellar-mass compact binaries, modulated by the slowly varying antenna pattern. This extended, modulated inspiral improves source reconstruction (especially sky localization) for systems that eventually merge in the LIGO–Virgo–KAGRA (LVK) band.

While the European Space Agency (ESA)-led LISA mission will explore the low-frequency mHz domain, it primarily targets massive black hole binaries, extreme mass ratio inspirals, and galactic compact binaries. Although LISA will also observe stellar-mass BBHs that will later merge in the LIGO band (e.g., systems similar to GW150914 [1, 2]), such sources will take several years to transition from the LISA band to the LIGO band. In contrast, a detector operating in the dHz regime would track the same systems only hours to days before merger, making it far more practical for generating timely early-warning alerts and enabling coordinated observations. Thus, a dHz detector naturally complements both LISA and the ground-based network, bridging the observational gap and enhancing the scientific return of the global GW effort.

In this context, we study a space-based gravitational-wave observatory concept, tentatively called **IndIGO-D**, developed under the auspices of the Indian Initiative in Gravitational-Wave Observations (IndIGO) consortium [20, 21]. We focus on a specific realization of IndIGO-D, consisting of three spacecraft flying in formation in a heliocentric orbit to form an L-shaped interferometer with 1000 km arms defined by the vertex–end separations and operating in the dHz band. While other realizations, including geocentric configurations of the spacecraft, are also possible within the IndIGO-D concept, all results presented here pertain to the heliocentric L-shaped geometry.

The scientific opportunities offered by GW observations in the dHz band have motivated several detector concepts. Prominent examples include DECIGO [22–24], TianGO [18], Lunar Gravitational-Wave Antenna (LGWA) [25–27] and Laser Interferometer Lunar Antenna (LILA) [28, 29]. DECIGO consists of four clusters of independent interferometric observatories orbiting in a heliocentric orbit. LGWA concept is based on the deployment of highly sensitive seismometers or inertial sensors on the lunar surface to measure the tiny tidal deformations induced by GWs. LILA will be an interferometric observatory on the lunar surface, leveraging the Moon’s exceptionally low seismic and Newtonian noise environment.

The dHz band hosts compact binaries whose signals remain in the band long enough to enable precise tracking, yet evolve quickly enough to permit actionable early-warning localization. Access to this frequency range would allow high-fidelity measurements of stellar-mass binaries, tighter constraints on compact-object populations, and improved prospects for multi-messenger observations. By combining the well-characterized Michelson geometry with the low-noise advantages of a heliocentric orbit, IndIGO-D would open an observational window between the mHz and terrestrial bands.

We outline the detector configuration and derive the stable spacecraft orbits in Sec. II. In Sec. III, we compute the full frequency-dependent antenna response, including long-baseline propagation effects and Doppler modulation from the orbital motion. In Sec. IV A, we estimate horizon distances for a broad range of compact binary sources using the projected sensitivity and compare the reach of IndIGO-D with that of existing and proposed observatories. We highlight several scientific opportunities that will be opened up by IndIGO-D, namely, prospects of multiband observations of BNS systems in Sec. IV B; detectability of intermediate-mass BBHs in Sec. IV C; and studying environmental effects and orbital eccentricity in Sec. IV D. Finally, we evaluate its early-warning capabilities through Bayesian parameter-estimation studies of simulated signals from a GW170817-like BNS system in Sec. IV E. In Sec. V, we present our conclusions and discuss future directions.

II. DETECTOR’S GEOMETRY AND ORBITAL CONFIGURATION

In the baseline configuration outlined earlier, the vertex spacecraft follows an Earth-like heliocentric orbit in the

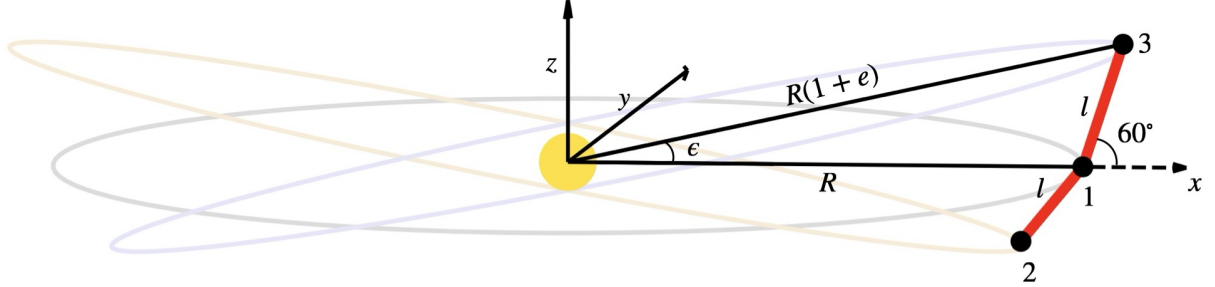


FIG. 1. The orbits of the three spacecraft constituting IndIGO-D. The spacecraft 1 at the vertex orbits the Sun in ecliptic plane at a distance of 1 AU, while the orbits of spacecraft 2 and 3 are inclined by 60° with respect to ecliptic which results in the most stable flight configuration such that the inter-spacecraft separation remain nearly constant throughout the motion.

ecliptic plane, leading Earth by about 20° in the same orbital path (see Fig. (1)). The orbits of the other two spacecraft are inclined with respect to the ecliptic such that the two lines joining each spacecraft to the vertex spacecraft remain perpendicular to each other, thereby creating an L-shaped geometry.

However, it is difficult to maintain a constant inter-spacecraft separation during the orbital path of the constellation. In the context of LISA, Dhurandhar et al. [30] described that the inter-spacecraft separation remains most stable along the flight when the plane of the constellation is tilted by 60° with respect to the ecliptic. We use this result and adapt it for an L-shaped configuration to find the orbits of the spacecraft forming the IndIGO-D detector.

The proposed orbits are such that the inter-spacecraft separation remains fixed to first order in the small dimensionless parameter $\alpha = l/2R \approx 3.34 \times 10^{-6}$, where l is the arm-length and R is the orbital radius of the vertex spacecraft. In this study, we ignore the contribution of gravitational interactions with other heavenly objects that will affect the motion of the constellation.

The vertex spacecraft follows a circular trajectory in the ecliptic plane ($x - y$ plane in Fig. (1)) and the orbit equation in terms of the coordinates (x_1, y_1) in the solar system barycenter (SSB) frame are given by,

$$x_1 = R \cos(\omega t), \quad y_1 = R \sin(\omega t), \quad z_1 = 0. \quad (1)$$

where, $R = 1$ AU denotes the orbital radius, ω denotes the orbital frequency of the vertex spacecraft and t is the time. The orbits of the other two spacecraft must be eccentric and inclined by 60° with respect to ecliptic plane to result in a fixed arm-length configuration up to first order in α .

The orbit of the spacecraft lying at one end of the

right-angled triangle (spacecraft 2) is given by,

$$\begin{aligned} x_2 &= R(\cos \psi_2 + e) \cos \epsilon, \\ y_2 &= R\sqrt{1 - e^2} \sin \psi_2, \\ z_2 &= R(\cos \psi_2 + e) \sin \epsilon, \end{aligned} \quad (2)$$

where, the eccentric anomaly ψ_2 satisfies,

$$\psi_2 + e \sin \psi_2 = \omega t. \quad (3)$$

The orbit of spacecraft 3 lying at the other end of the right-angled triangle is given by,

$$\begin{aligned} x_3 &= -R\sqrt{1 - e^2} \sin \psi_3, \\ y_3 &= R(\cos \psi_3 + e) \cos \epsilon, \\ z_3 &= R(\cos \psi_3 + e) \sin \epsilon, \end{aligned} \quad (4)$$

where, ψ_3 is given by the solution to the following equation,

$$\psi_3 + e \sin \psi_3 = \omega t - \frac{\pi}{2}. \quad (5)$$

The orbital inclination ϵ can be obtained from the geometry and is given by,

$$\tan \epsilon = \frac{\frac{\sqrt{3}l}{2R}}{1 + \frac{l}{2R}} = \frac{\sqrt{3}\alpha}{1 + \alpha}, \quad (6)$$

This corresponds to the orbital inclination, $\epsilon \approx 5.79 \times 10^{-6}$. The orbital eccentricity, e , can be obtained by solving $R^2(1+e)^2 = (\sqrt{3}l/2)^2 + (R+l/2)^2$,

$$e = \sqrt{1 + 2\alpha + 4\alpha^2} - 1 \approx 3.34 \times 10^{-6}. \quad (7)$$

The time evolution of the spacecraft orbits can be computed by substituting ψ_2 , ψ_3 , ϵ and e into Eqs. (1), (2), and (4).

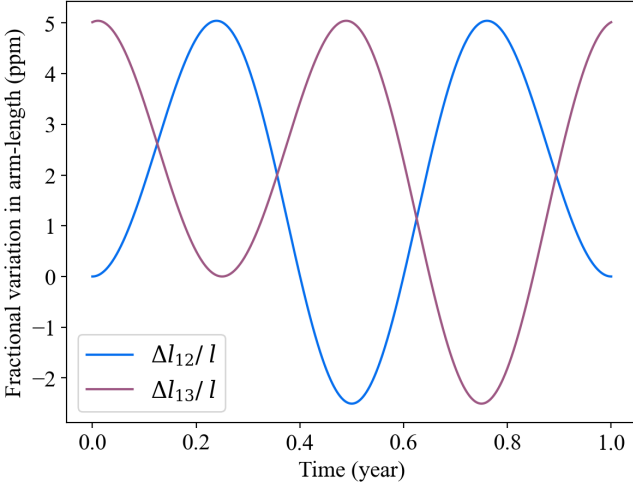


FIG. 2. Flexing of the arms: fractional variation of the inter-spacecraft separation (computed using the approximated orbits described by Eq. (8)) along the two arms over one orbital period of the constellation. The separation varies by ~ 7.5 m over a drift timescale $t_{\text{drift}} \sim \mathcal{O}(\text{months})$ within a single orbital period.

The exact orbits of the three spacecraft result in a slight variation in the arm-length along the trajectory. Fig. (2) shows the variation in the inter-spacecraft separations in one full orbital period of the constellation.

To first order in α , Eq. (6) and Eq. (7) imply that $\epsilon \approx \sqrt{3}\alpha$ and $e \approx \alpha$ and the eccentric anomalies ψ_2 and ψ_3 for the two spacecraft orbits become,

$$\begin{aligned}\psi_2 &= \omega t - e \sin(\omega t), \\ \psi_3 &= (\omega t - \pi/2) - e \sin(\omega t - \pi/2).\end{aligned}\quad (8)$$

These expressions when substituted into Eqs. (2) and (4), result in a constant inter-spacecraft separation l along the trajectory.

III. ANTENNA PATTERN FUNCTIONS

Antenna pattern functions describe the directional sensitivity of the detector towards the two polarizations of the GWs. Due to longer in-band duration of the GW signal, the antenna pattern will not be static. Moreover, due to large interferometric arms, the finite detector size effects will also be non-ignorable. In this section, we describe the time and frequency dependent antenna pattern functions for the envisioned IndIGO-D detector. For the dHz detector configuration we study here, the two interferometric baselines form orthogonal arms of length l_1 and l_2 that meet at the vertex spacecraft. We denote by

\hat{l}_1 and \hat{l}_2 the unit vectors pointing away from this vertex; they satisfy $\hat{l}_1 \cdot \hat{l}_2 = 0$ and $|\hat{l}_1| = |\hat{l}_2| = 1$, and specify the instantaneous orientations of the two arms. The vertex spacecraft, located at \vec{x}_1 in the SSB frame, serves as the laser transmitter for the other two spacecraft.

Using Eq. (A4), the phase shift recorded at the output port of the Michelson interferometer is given by,

$$\begin{aligned}\Delta\tilde{\phi}(f; t) &= \tilde{\phi}_1(f; t) - \tilde{\phi}_2(f; t) \\ &= 2\pi e^{-2\pi i f \hat{k} \cdot \vec{x}_1/c} \tilde{h}_{ij}(f) \left[l_1 \hat{l}_1^i \hat{l}_1^j \mathcal{T}_1 - l_2 \hat{l}_2^i \hat{l}_2^j \mathcal{T}_2 \right]\end{aligned}\quad (9)$$

where,

$$\mathcal{T}_1 \equiv \mathcal{T}(\hat{l}_1 \cdot \hat{k}, f; t), \quad \mathcal{T}_2 \equiv \mathcal{T}(\hat{l}_2 \cdot \hat{k}, f; t),$$

are the single-arm transfer functions as shown in Eq. (A5). This factor encodes the finite light-travel time along the arm and the projection of the GW on the arm direction.

In Appendix A we quantify the effect of the few-ppm arm-length drift that occurs over a timescale of several months. At the leading order, this drift introduces an $\mathcal{O}(10^{-6})$ fractional correction to the Michelson phase response, which is negligible. This level of variation is well below typical calibration uncertainties [31] in advanced LIGO detectors and systematic errors [32] in state of the art waveform models. For context, although LISA is a distinct mission with $\sim 10^9$ m arms and a different interferometric geometry, its calibration studies [33] indicate strain-reconstruction uncertainties of $\mathcal{O}(10^{-3}\text{--}10^{-2})$, providing a useful reference scale for calibration systematics in space-based interferometers. We therefore treat the arms as having fixed and equal length l , i.e., $l_1 = l_2 = l$.¹

With this simplification, Eq. (9) can now be written as,

$$\begin{aligned}\Delta\tilde{\phi}(f; t) &= 2\pi l e^{-2\pi i f \hat{k} \cdot \vec{x}_1/c} \tilde{h}_{ij}(f) \left[\hat{l}_1^i \hat{l}_1^j \mathcal{T}_1 - \hat{l}_2^i \hat{l}_2^j \mathcal{T}_2 \right] \\ &= 4\pi l e^{-2\pi i f \hat{k} \cdot \vec{x}_1/c} D^{ij}(\hat{l}_1, \hat{l}_2, \hat{k}, f; t) \tilde{h}_{ij}(f) \\ &= 4\pi l \tilde{h}(f; t),\end{aligned}\quad (10)$$

where, D^{ij} is the detector tensor:

$$D_{ij}(\hat{l}_1, \hat{l}_2, \hat{k}, f; t) := \frac{1}{2} \left(\hat{l}_1^i \hat{l}_1^j \mathcal{T}_1 - \hat{l}_2^i \hat{l}_2^j \mathcal{T}_2 \right), \quad (11)$$

and where $\tilde{h}(f; t) \equiv D^{ij} \tilde{h}_{ij}$ is the effective induced strain recorded in the detector.

¹ In practice, a small fixed difference in the arm-length, known as Schnupp asymmetry [15], maybe maintained in the interferometer, which we are not considering here for this theoretical study.

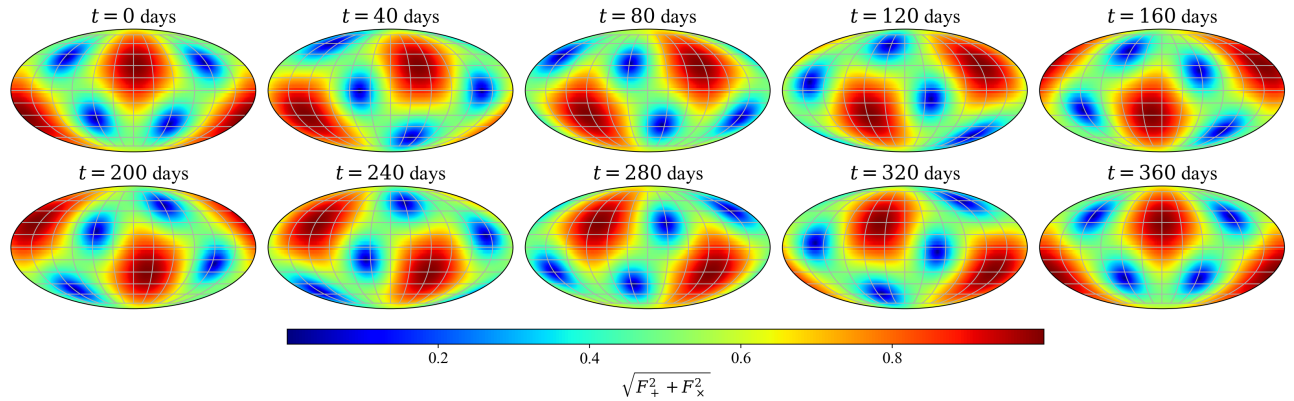


FIG. 3. Variation in the magnitude of the antenna pattern functions across the whole sky in nearly one orbital period of the spacecraft constellation, assuming long-wavelength limit. Grids in the sky-map correspond to the ecliptic longitude and ecliptic latitude that marks the position in the sky in the SSB frame. Note that at any instant there exists 4 blind and 2 bright spots where the magnitude of antenna patterns are 0 and 1, respectively. The 4 blind spots lie in the detector's plane along the lines making an angle of 45° with the detector's arms. The 2 bright spots lie perpendicular to the detector's plane, above and below the detector.

For the 1000 km arm IndIGO-D dHz detector concept, the light-travel time along one arm is $t_{\text{light}} \simeq 3 \times 10^{-3}$ s. In this band, the GW period is on timescales of order $t_{\text{GW}} \sim 1$ to 10 s. As shown in Fig. (2), the arm-length drift occurs on month-scale times, $t_{\text{drift}} \sim 10^6$ – 10^7 s. This establishes a clear hierarchy $t_{\text{drift}} \gg t_{\text{GW}} \gg t_{\text{light}}$, under which the arm-length variations act only as a slow, multiplicative modulation of the Michelson response. The interferometer is effectively rigid on light-propagation timescales and adiabatic on the timescale of the GW oscillation, so the drift contributes only a negligible, slowly varying correction to the instantaneous response.

Expanding the metric perturbation \tilde{h}_{ij} in the polarization basis $e_{ij}^{+,\times}(\hat{k}, \psi)$ (See Eqs. (A2) and (A3)), the induced strain in the detector can be written as a linear combination of the GW polarization amplitudes $\tilde{h}_{+,\times}(f)$:

$$\tilde{h}(f; t) = e^{-2\pi i f \hat{k} \cdot \vec{x}_1 / c} \sum_{a=+,\times} F_a(\hat{k}, \psi, f; t) \tilde{h}_a(f). \quad (12)$$

Here $F_{+,\times}$ are the antenna pattern functions, defined by the contraction of the detector tensor with the corresponding polarization tensors:

$$F_+(\hat{k}, \psi, f; t) = D^{ij}(\hat{l}_1, \hat{l}_2, \hat{k}, f; t) e_{ij}^+(\hat{k}, \psi), \quad (13)$$

$$F_\times(\hat{k}, \psi, f; t) = D^{ij}(\hat{l}_1, \hat{l}_2, \hat{k}, f; t) e_{ij}^\times(\hat{k}, \psi). \quad (14)$$

The antenna pattern functions have explicit dependence on time and frequency due to time-varying spacecraft positions and finite detector size effects, respectively. However, in the long wavelength limit (LWL), when the wavelength of the observed GW signal is very large in

comparison to the length of the detector arms ($\lambda_{gw} \gg l$, or, equivalently the frequency $f_{gw} \ll c/2\pi l$), the transfer functions given by Eq. (A5) approaches unity; and the antenna patterns become only time-dependent.

Fig. (3) illustrates how the combined magnitude of the '+' and the '×' antenna patterns varies across the sky, assuming the long-wavelength limit, over one orbital period of the constellation.

As the source parameter estimation analysis is performed in the frequency domain due to cleaner noise modeling and more efficient likelihood evaluation, it is desirable to generate the detector frame waveforms completely in the frequency domain. The complete antenna response can be computed in the frequency domain by utilizing the time-frequency correspondence associated with the binary in a stationary phase approximation,

$$t(f) = t_c - \frac{1}{2\pi} \frac{d\Psi(f)}{df}, \quad (15)$$

where, $\Psi(f)$ is the GW phase and t_c is the coalescence time. For a given set of intrinsic parameters, at any given instantaneous frequency f the corresponding epoch t can be evaluated using Eq. (15). Thus, the time-dependent quantities in the response function can be evaluated corresponding to a given frequency and the waveform can be computed directly in the frequency domain.

Fig. (8) shows the comparison of the antenna response function with and without assuming LWL, evaluated entirely in the frequency domain using time-frequency mapping given by Eq. (15) for a GW170817 like compact binary system. Various time stamps before the merger

are also shown in the plot. The initial modulation in the low-frequency regime corresponds to the changing orientation and position of the detector. The antenna pattern factors calculated with and without assuming LWL exhibit disagreement towards the higher-end of the frequency spectrum where the finite detector size effects become important and the transfer functions (given by Eq. (A5)) deviates significantly from unity. Note that the antenna pattern functions *without LWL* are complex valued because of the transfer functions.

IV. SCIENCE CAPABILITIES OF INDIGO-D

Third-generation (3G) ground-based detectors such as Cosmic Explorer (CE) and the Einstein Telescope (ET) are designed to extend their sensitivity to lower frequencies than the current detector network, with CE reaching a low-frequency cutoff of approximately 5 Hz and ET extending down to about 2 Hz. These upgrades are expected to extend the observable inspiral of BNS systems to tens of minutes to hours before merger. Nevertheless, even 3G instruments cannot overcome the seismic barrier below a few Hz, leaving a substantial region of astrophysically informative signal cycles inaccessible from the ground. The proposed IndIGO-D space-based mission would specifically target this low-frequency gap with sensitivity spanning 0.1 to 30 Hz.

While the final design sensitivity for IndIGO-D will depend on various parameters, here we use a fiducial (one-sided) noise power spectral density (PSD) [35] given by:

$$S_n(f) = A_{\text{acc}} \left(\frac{f}{f_l} \right)^{-4} + A_{\text{shot}} \left[1 + \left(\frac{f}{f_u} \right)^2 \right], \quad (16)$$

where $A_{\text{acc}} = 13.10 \times 10^{-46} \text{ Hz}^{-1}$, $A_{\text{shot}} = 18.47 \times 10^{-46} \text{ Hz}^{-1}$, and $f_l = 0.1 \leq f \leq f_u = 30 \text{ Hz}$ is the putative bandwidth of the IndIGO-D detector. The sensitivity curve is plotted in Fig. (4a) and seems reasonable for studying the scientific advantage of such a detector. An “L” shaped Michelson interferometer with $\sim 1000 \text{ km}$ armlength and a $\sim 10 \text{ W}$ laser with $\sim 1 \mu\text{m}$ wavelength may be able to provide such a level of sensitivity.

Fig. (4a) shows the noise amplitude spectral densities (ASD) of various detectors, $\sqrt{S_n(f)}$, as well as the ASD of GW signals, $2\sqrt{f}\tilde{h}(f)$, as a function of GW frequency. The ASD of the GW170817-like signal is represented by the solid black curve, with filled red circles marking the corresponding times before merger at selected frequencies. For comparison, the gray dashed

curve shows the frequency evolution of the GW150914-like BBH system across the same frequency range. Here, the waveforms are generated using the `IMRPhenomD` waveform approximant [36].

A GW170817-like BNS system within the IndIGO-D band would be detectable for several years prior to coalescence, enabling continuous monitoring throughout the slow early inspiral during which the majority of signal cycles accumulate. Such a system would enter the ET sensitivity band at 2 Hz only about a day before merger and the CE band at 5 Hz about two hours prior to coalescence. Access to this prolonged low-frequency inspiral enables multi-band detection and a significant improvement in both early-warning notice and sky localization precision.

A. Horizon Distances for Coalescing Compact Binary Sources

The sensitivity of a GW detector to compact binaries is characterized by the horizon distance, defined as the farthest luminosity distance at which a source produces a signal-to-noise ratio (SNR) of 8, assuming optimal orientation (face-on) and sky location. For a frequency-domain waveform $\tilde{h}(f)$, the SNR ρ is given by

$$\rho^2 = 4 \int_{f_{\text{low}}}^{f_{\text{high}}} \frac{|\tilde{h}(f)|^2}{S_n(f)} df, \quad (17)$$

where $S_n(f)$ is the one-sided noise PSD of the detector and $f_{\text{low}} \leq f \leq f_{\text{high}}$ is the detector bandwidth. For a source detected at redshift z , the corresponding source-frame mass is related to the detector-frame mass through $M_{\text{source}} = M_{\text{observed}}/(1+z)$. The conversion between luminosity distance and redshift depends on the assumed cosmology. In this work, we adopt the Planck 2018 [37] Λ CDM cosmology as implemented in `Astropy`.

Fig. (4b) illustrates, for each detector, the farthest distance and corresponding redshift at which a symmetric, non-spinning compact binary of a given total source-frame mass could be observed. To illustrate variations in detector response due to the sky location of the source, we evaluate the maximum detectable distances for 48 uniformly distributed sky positions. The upper solid line denotes the horizon distance for the most favorable sky position. The dark-shaded band encloses the luminosity distance within which 50% of these sky position sources produce an SNR above the nominal threshold of 8, while the lighter-shaded region extends to the distance covering 90% of detections. In this calculation, we consider a maximum in-band duration of 5 years.

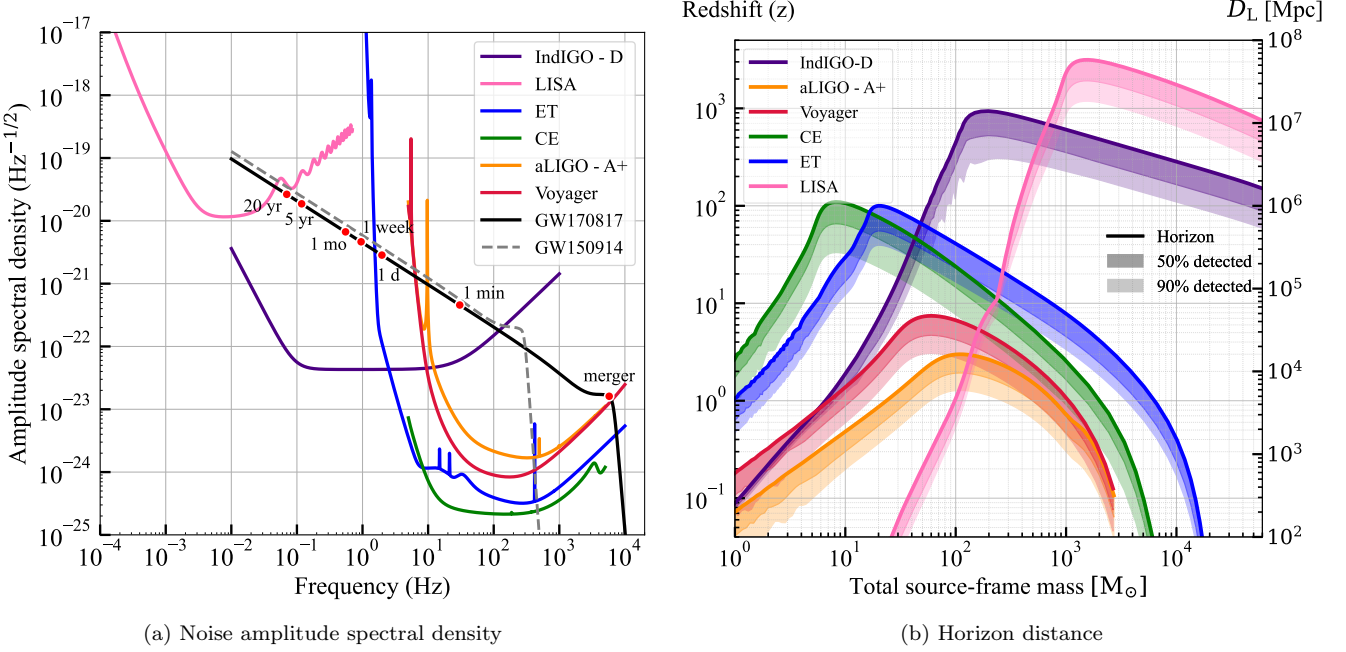


FIG. 4. Comparison of detector sensitivities and horizon distances. Note that IndIGO-D is sensitive to binary neutron star systems out to a horizon distance of ~ 1000 Mpc, similar to LIGO-Voyager [34].

(a) Noise sensitivities: Detector noise amplitude spectral densities (ASD) for various detectors, along with the ASD of the GW170817- and GW150914-like GW signals, given by $2\sqrt{f}\bar{h}(f)$. The red-filled circles represent the time before the merger at a specific GW frequency.

(b) Horizon distance (right axis) and corresponding redshift (left axis) as functions of source-frame total mass for equal-mass compact binaries. Detection distances are evaluated for 48 uniformly distributed sky positions, with the inclination angle fixed to zero (face-on). The upper solid line indicates the horizon distance, while the dark and light shaded bands indicate the distances enclosing 50% and 90% of sky locations, respectively.

For a GW170817-like BNS system, Advanced LIGO with A+ sensitivity [38] would reach a horizon redshift of approximately 0.15, which corresponds to ~ 750 Mpc. The 3G detectors would significantly extend this reach, with ET achieving $z \sim 4$ and CE reaching $z \sim 15$. The dHz space mission IndIGO-D attains a horizon redshift of $z \sim 0.3$. Within this overlapping redshift range $z \lesssim 0.3$, IndIGO-D will observe several years of the early inspiral of a BNS system, thereby providing precise constraints on source parameters before the system becomes detectable by terrestrial observatories. This enables coherent multi-band measurements of these sources when they later enter the ET and CE sensitivity bands.

B. Multiband Access to BNS Sources: IndIGO-D and 3G Detectors

Although the horizon redshift corresponds to an optimally located and face-on binary, real astrophysical binaries are distributed isotropically in both orientation

and sky position. The inclination angle strongly influences the observed GW amplitude through the $(1 + \cos^2 \iota)$ and $\cos \iota$ dependencies of the plus and cross polarizations, which lowers the effective detection reach relative to the idealized horizon value. To quantify the impact of non-zero inclination and sky location on detectability and to assess the prospects for multi-band observations, we simulate a population of 10^4 BNS systems with component source-frame masses of $1.4 M_\odot$. The binary population is generated assuming isotropic inclination angles and a uniform distribution over the sky in celestial coordinates for LIGO-Voyager, which are subsequently transformed into the SSB frame for IndIGO-D. The source redshifts are drawn uniformly in comoving volume up to $z = 0.33$, which corresponds to the approximate horizon for face-on systems for IndIGO-D as shown in Fig. (4b).

For each simulated binary, we compute the SNR in both LIGO-Voyager and IndIGO-D and determine the fraction of sources that satisfy $\rho \geq 8$. As shown in Fig. (5), approximately 18% of the sources are detectable by IndIGO-D and 26% by Voyager. All sources detected

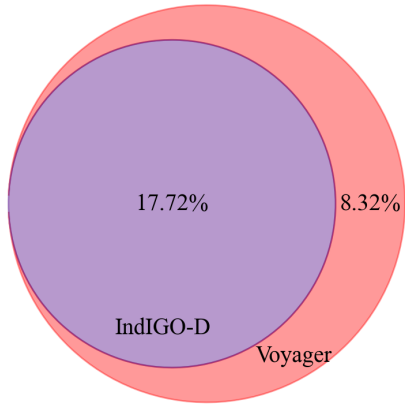


FIG. 5. Detection fractions ($\text{SNR} \geq 8$) for simulated merging binary neutron star systems with component masses $(1.4, 1.4) M_{\odot}$, isotropic orientations, and a population distributed uniformly in comoving volume out to $z = 0.33$. IndIGO-D and Voyager detect 17.72% and 26.04% of the sources, respectively. All sources detected by IndIGO-D will also be detected by Voyager. The overlap illustrates the multi-band science potential, in which IndIGO-D provides long-duration tracking and pre-merger localisation in the dHz band for events later observed in the Voyager band.

by IndIGO-D are also detected by Voyager, so the multi-band observable samples coincide with the full IndIGO-D detection set. This demonstrates that, even after incorporating a realistic distribution of inclination angles and sky positions, a significant fraction of BNS systems within $z \leq 0.33$ remain jointly detectable in dHz and ground-based detector bands. IndIGO-D therefore provides strong multi-band capability when paired with Voyager or other future ground-based interferometers.

C. Observational Reach for Intermediate-Mass Black-Hole Systems

Another key target population for IndIGO-D consists of IMBHs with total masses in the range 10^2 – $10^5 M_{\odot}$. For a nonspinning black hole of mass M , the GW frequency associated with the innermost stable circular orbit (ISCO) is

$$f_{\text{ISCO}} \approx 4.4 \text{ Hz} \left(\frac{M}{1 \times 10^3 M_{\odot}} \right)^{-1}, \quad (18)$$

which scales inversely with the total mass. This implies that binaries with total masses 10^2 – $10^4 M_{\odot}$ radiate their late-inspiral and merger signal in the dHz band. In this mass regime, LISA observes only the slow, very early inspiral because its sensitivity declines above ~ 0.1 Hz, while terrestrial detectors such as Advanced LIGO and ET

become sensitive to frequencies above ~ 10 Hz and ~ 1 Hz, respectively. The gravity-gradient noise barrier around 1 Hz prevents ground-based detectors from detecting these systems at high redshifts. Consequently, probing the mass interval 10^2 – $10^3 M_{\odot}$ robustly requires a detector optimized for the dHz band. IndIGO-D fills this observational gap precisely. Its sensitivity would enable the detection of mergers between two IMBHs as well as intermediate-mass-ratio inspirals in which a stellar-mass compact object inspirals into an IMBH.

The coalescence of an equal-mass binary with a source-frame total mass of $10^3 M_{\odot}$ remains detectable up to redshift $z \sim 600$ as shown in Fig. (4b). This reach exceeds that of both current and planned ground-based detectors for systems in this mass range and complements LISA’s ability to follow their earlier, low-frequency evolution in the mHz band. The astrophysical implications of such observations are substantial. Many formation scenarios for supermassive black holes posit an intermediate-mass phase during which BH seeds grow through mergers and accretion [39, 40]. The direct detections of IMBH mergers would therefore provide valuable insight into the early formation of massive BHs and the dynamical environments, such as dense star clusters and galactic nuclei, that host them.

D. Probing Environmental Effects and Orbital Eccentricity

Observations in the dHz band also offer a unique opportunity to probe the dark matter (DM) environments surrounding compact binaries. If a compact object resides within a dense distribution of DM, for example within a spike formed by the adiabatic growth of an IMBH [41–43] or within an overdensity produced around a primordial BH seed [44, 45], the surrounding matter can produce subtle modifications to the gravitational waveform [46–49]. Effects such as dynamical friction and particle accretion modify the inspiral rate and produce small phase shifts relative to the vacuum prediction [50–53]. Although each of these effects are individually weak, their influence accumulates over the many orbital cycles that a binary spends in the dHz band, making long-duration observations particularly sensitive to such perturbations. IMRIs with primary masses in the range $m_1 \sim 10^3$ – $10^5 M_{\odot}$ and secondary masses $m_2 \sim 1$ – $10 M_{\odot}$, which emit GWs at $f_{\text{GW}} \sim 0.1$ – 10 Hz during the final years of inspiral, are particularly promising targets. IndIGO-D’s sensitivity in this regime allows it to detect or place strong constraints on the presence of DM spikes

surrounding IMBHs [54]. A definitive measurement of such an overdensity would shed light on the distribution and nature of particle DM in the vicinity of compact objects.

Another important capability of IndIGO-D would be the measurement of binary orbital eccentricity, a parameter that is difficult to constrain with ground-based detectors. Eccentricity is a key characteristic that helps differentiate between the formation processes of BBHs [55], whether they are formed in isolation or through dynamical interactions. Compact binaries formed in dense stellar environments, such as globular clusters, can retain significantly higher eccentricities than those produced through isolated binary evolution in galactic fields [56]. Most binaries observable above ~ 10 Hz are expected to be nearly circular due to efficient GW-driven circularization [57]. Compact binary systems in the dHz band may, however, retain measurable residual eccentricity from their formation channel. The significant eccentricity of compact binaries emitting GWs may have an impact on the observable properties within the sensitivity range of ground-based and space-based detectors [58–60].

E. IndIGO-D: Early warning capabilities

Pre-merger localization of compact binary sources is crucial to not only capture the short-lived and highly beamed gamma-ray emission that decays within a few seconds right after the merger [61], but may also be important for any possible pre-merger EM emissions in binary evolution [62–66]. The temporal and spectral properties of the early gamma-ray emission provide direct constraints on the formation and structure of the relativistic jet launched at merger. These observations inform models of jet energetics, angular structure, Lorentz factors, and magnetic-field configurations, thereby probing the physics of the merger remnant and jet-launching mechanisms [67].

A key advantage of a dHz detector is the long in-band residence time of compact binaries that will later merge in the band of terrestrial GW observatories. For BNS systems, the signal enters the IndIGO-D band several months before coalescence, allowing coherent SNR to build up well in advance of the merger. Moreover, longer in-band duration will result in Doppler modulations in the observed GW signal in IndIGO-D, which will facilitate improved sky localization of such sources. We therefore expect IndIGO-D to provide useful pre-merger localization for nearby BNS sources, with sky areas shrinking steadily

as more of the low-frequency inspiral is accumulated.

To quantify the early-time localization performance with IndIGO-D, we inject a GW170817-like GW signal using `IMRPhenomD_NRTidalv2` [68, 69] waveform approximant with parameters corresponding to the maximum a posteriori (MAP) values of the posterior estimates of the real event as obtained from [70], assuming stationary, Gaussian noise colored with the PSD. The sky position is transformed from the geocentric estimates into the SSB frame while generating the simulated data. For this analysis, we consider $f_{\min} = 0.36$ Hz and $f_{\max} = 30$ Hz so that the total duration of the signal is 3 months in IndIGO-D. We perform parameter estimation analyses in 13-dimensional parameter space for four distinct epochs before merger, namely, 1 month, 1 week, 1 day and 6 hours that correspond to f_{\max} of 0.55, 0.95, 1.97, and 3.32 Hz, respectively. As mentioned in Appendix B, we use relative binning [71–73] to accelerate the likelihood computation while sampling and use the true injection parameters as the fiducial reference waveform parameters.

Fig. (6) shows the sky-localization area corresponding to the 90% CI of the posterior distributions obtained for each analysis. Various epochs corresponding to distinct look-back times for which analysis is performed are also represented by dots in the time-frequency track of the binary. The time-frequency track is colored by the accumulated SNR in the IndIGO-D starting from $f_{\min} = 0.36$ Hz. The values of the SNR accumulated till 1 month, 1 week, 1 day and 6 hours before merger in IndIGO-D are 82.4, 96.8, 102.5 and 104.2, respectively.

We find that IndIGO-D can localize a binary-neutron-star source to an area of $\sim 21, \text{deg}^2$ one month before merger. This improves to $\sim 1.6, \text{deg}^2$ one week prior to merger, and shrinks further to $\sim 0.4, \text{deg}^2$ at one day and $\sim 0.3, \text{deg}^2$ at six hours before coalescence. These results are summarized in Table I.

For comparison, we compute the sky-localization area for the same source as will be observed in ET and a network of four second generation detectors LIGO-Aundha, Hanford, Livingston, and Virgo (AHLV) at their design sensitivity. For ET, we take a lower cut-off frequency f_{\min} of 2 Hz, and generate the simulated data assuming stationary, Gaussian noise colored with ET PSD, upto the epoch of 6 hours prior to merger, which corresponds to $f_{\max} = 3.32$ Hz. The total in-band duration for the considered frequency interval is ~ 17 hours. A good sky localization is expected due to the induced modulation in the accumulated signal because of the rotation of the Earth. The total accumulated SNR is 32.5 considering three channels of ET corresponding to three independent interferometers. It results in the

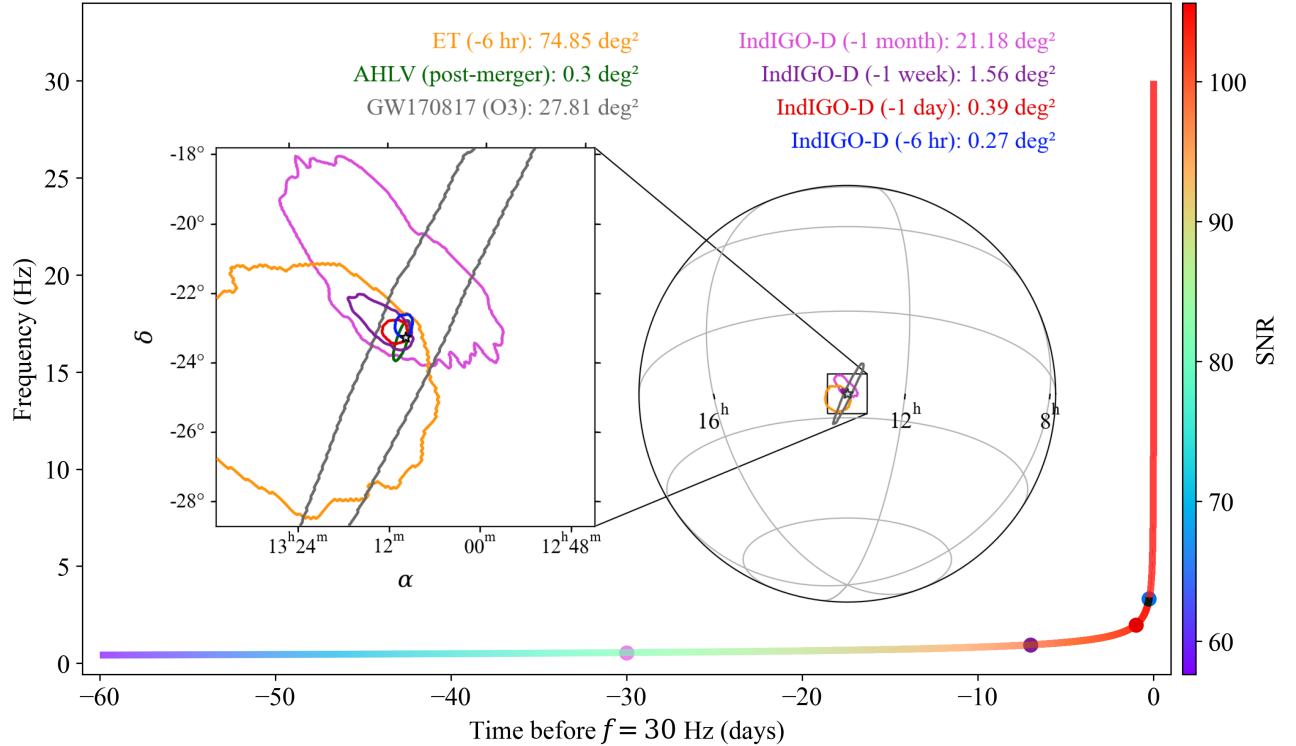


FIG. 6. Sky-localization area (90% credible interval) for a GW170817-like binary neutron star at different pre-merger epochs in simulated IndIGO-D data: one month, one week, one day, and six hours before merger. For comparison, we also show the localization obtained with ET at six hours before merger and the post-merger localization with the AHLV network at design sensitivity. For reference, the localization patch for the real GW170817 event observed by the HLV network during the O3 run is included. The ET sky posterior is bimodal; only the dominant mode is shown, with the secondary mode located on the opposite side of the sky. The corresponding epochs are indicated on the time–frequency track of the binary, which is colored by the accumulated signal-to-noise ratio over the three-month in-band evolution in IndIGO-D up to 30 Hz.

localization area of ~ 75 deg 2 at the 6 hours pre-merger epoch. For AHLV network, we take f_{\min} to be 10 Hz and simulate data till the merger. It results in the localization area of 0.3 deg 2 . In Fig. (6), we also show the sky-localization contour for GW170817 derived from publicly available posterior samples from Romero-Shaw et al.’s independent reanalysis of the GWTC-1 compact binary merger events using the Bilby Bayesian inference framework. This is not an LSC/Virgo Collaboration analysis, but an independent inference performed using open data and open-source tools [70].

The dHz band provides substantially earlier directional information than existing or 3G high-frequency detector networks, indicating the potential of IndIGO-D for actionable pre-merger alerts and coordinated electromagnetic follow-up.

Electromagnetic follow-ups

Studies by Nissanke et al. [74] have shown that large optical telescopes with wide fields of view and deep limiting magnitudes are essential for unambiguous identification of electromagnetic counterparts to GW mergers. In our design study, IndIGO-D can localize binary neutron star mergers to areas of $\lesssim 10$ deg 2 in the final few days before the signal enters the ground-based band which can be readily tiled by wide-field gamma-ray and optical telescopes. For example, the field of view (FoV) of Large Area Telescope (LAT), the primary instrument on the Fermi gamma-ray space telescope is ~ 7878 deg 2 [75]. And, the Rubin Observatory/LSST, with an 8.4-m aperture and a 9.6 deg 2 FoV per pointing, can reach a single-visit depth of $r \simeq 24.5$ for point sources [76], allowing the entire IndIGO-D localization region to be covered with only one to two pointings. For a GW170817-like kilonova with peak absolute magnitude $M_r \simeq -16$ [77], this back-of-the-envelope

Detector	Time to merger	f_{max} Hz	SNR	90% sky area deg^2
IndIGO-D	1 month	0.55	82.4	21.18
	1 week	0.95	96.8	1.56
	1 day	1.97	102.5	0.39
	6 hours	3.32	104.2	0.27
ET	6 hours	3.32	32.3	74.85
AHLV	post-merger	2048.00	84.2	0.30
HLV (O3)	post-merger	1024.00	32.4	27.81

TABLE I. Sky-localization area (90% credible interval) for a GW170817-like binary neutron star at different pre-merger epochs, obtained with IndIGO-D and representative terrestrial high-frequency detector networks. For IndIGO-D, the analysis spans frequencies from $f_{\text{low}} = 0.36$ Hz, corresponding to an in-band duration of ~ 3 months, up to 30 Hz. For ET, the analysis begins at 2 Hz, while for the Advanced LIGO–Virgo (AHLV) network at design sensitivity it begins at 10 Hz. For reference, we also show the post-merger sky-localization region of the real GW170817 event observed by the HLV network during O3. IndIGO-D achieves $\mathcal{O}(1)$ deg^2 sky localization up to a week before merger, enabling pre-merger electromagnetic follow-up and outperforming both advanced and third-generation high-frequency detector networks at early times.

scaling corresponds to a detection horizon of $D_L \simeq 1.26$ Gpc, or $z \approx 0.3$ in a standard cosmology; with high-cadence revisits providing even deeper stacked limits. These numbers demonstrate that IndIGO-D’s pre-merger localization capabilities are well matched to the field of view and depth of modern wide-field optical telescopes.

In an observational regime where multiple EM-bright compact binaries may be simultaneously detected, early chirp mass measurements from IndIGO-D can provide a powerful tool for prioritizing EM follow-up. Systems with chirp masses indicative of long-lived remnants or enhanced mass ejection can be identified well in advance of merger and flagged as high-priority targets for intensive monitoring. This capability is particularly valuable for capturing rapidly evolving or sharply decaying EM signals.

Fig. (7) shows that dHz GW observations enable an early and precise measurement of the chirp mass, with fractional uncertainties of $\mathcal{O}(10^{-6} – 10^{-5})$ achievable weeks to months prior to merger for a GW170817-like system. Such precision has direct implications for EM follow-up strategies. As emphasized by Margalit and Metzger [78], the chirp mass provides a strong discriminator of the BNS merger outcome such as prompt collapse to a black hole or the formation of a (temporary)

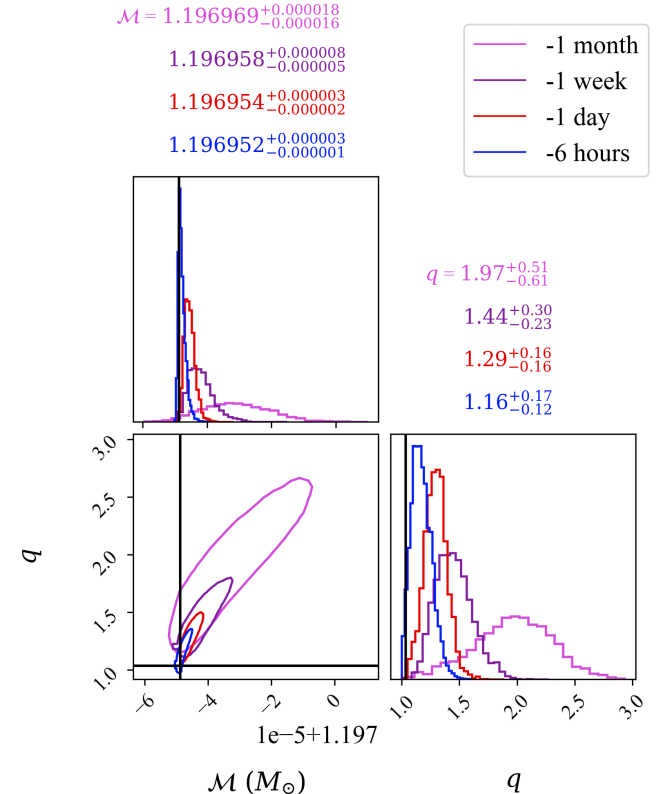


FIG. 7. Comparison of two-dimensional marginalized posterior distributions in chirp mass and mass ratio for a GW170817-like system, obtained from simulated IndIGO-D data at different epochs before merger, as indicated in the legend. The contours show the 90% credible regions, with colours matching those of the IndIGO-D early-warning skymaps in Fig. (6). As expected, parameter inference becomes progressively more accurate as the signal accumulates in-band. These results can be directly compared with the corresponding sky-localization performance shown in Fig. (6).

massive neutron-star remnant, which directly affects the amount of ejecta and the resulting electromagnetic emission.

IndIGO-D could thus play a crucial role in enabling efficient and targeted multi-messenger campaigns.

V. CONCLUSIONS AND OUTLOOK

In this work, we have analysed a specific heliocentric configuration of IndIGO-D, a community-led space-based interferometric gravitational-wave observatory concept developed within the IndIGO consortium and expected to operate in the decihertz band.

We provide a detailed description of the orbits of the spacecraft resulting in the most stable configuration of the

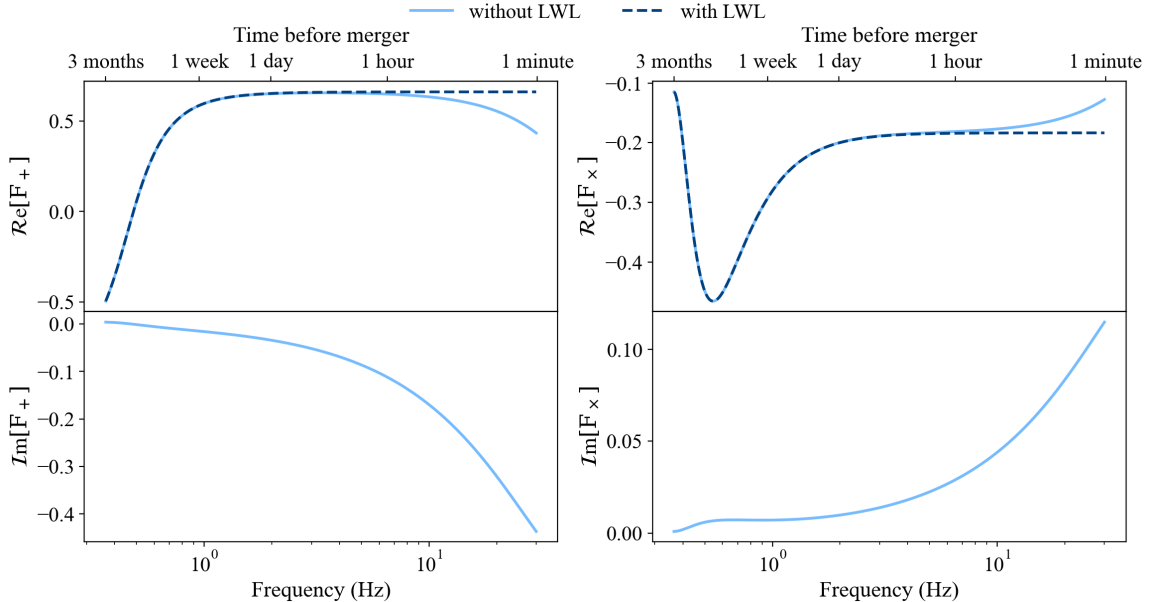


FIG. 8. Comparison of the antenna pattern functions corresponding to the two polarizations, with and without assuming the LWL, evaluated in the frequency domain for a GW170817 like system as a function of frequency. Consideration of finite detector size effects results in complex valued $F_{+,\times}$. The top and bottom panels correspond to the real and imaginary parts of $F_{+,\times}$. The modulation in the lower end of the frequency spectrum corresponds to the changing orientation and position of the detector as the binary radiates for a longer period of time in the lower frequency regime. As the inspiral rate increases, the time-dependent effects get suppressed and the antenna pattern functions become nearly constant in LWL (dashed dark blue curve). However, consideration of finite detector size effects results in modulated $F_{+,\times}$ at the higher end of the frequency spectrum (solid light blue curve).

detector. The resulting arm-length flexing is at the level of a few ppm, occurring on timescales of months. This orbital configuration induces a slow cartwheel-like rotation of the detector, providing full-sky coverage over the duration in which GW signals accumulate (see Fig. (3)), along with strong Doppler and amplitude modulation of long-lived inspiral signals in the dHz band.

We describe the full antenna pattern functions of the detector. The three spacecraft constellation behaves effectively as a rigid interferometer on GW evolution timescales. We demonstrate that the ppm-level arm-length drifts introduce only $\mathcal{O}(10^{-6})$ corrections to the response, implying that the equal-arm approximation is valid to extremely high accuracy for the purpose of waveform modeling and parameter estimation.

Using the projected sensitivity curve of IndIGO-D, we evaluate the horizon distances for a wide range of compact binary systems and compared them with the capabilities of LISA, 2G, and 3G observatories. IndIGO-D will observe the early inspirals of BNS systems out to a redshift of 0.3, that will later be observed by the LIGO Voyager or future 3G detectors such as the ET or CE, enabling multi-band observations.

At higher masses, IndIGO-D is sensitive to IMBHs with total masses in the $10^2 - 10^4 M_\odot$ range out to redshifts exceeding $z \sim \mathcal{O}(10^2)$ for equal mass ratios. Such a distance reach far surpasses that of both LISA and ground-based observatories and opens a new observational window onto the formation pathways of IMBHs. We also highlight the role of IndIGO-D in detecting effects of dark matter spikes around IMBHs and orbital eccentricities of compact binaries.

We quantify the early-warning capability of IndIGO-D using a detailed Bayesian inference study on simulated GW170817-like signal. We show that IndIGO-D can localize such sources within $\mathcal{O}(10)$ deg² one month, and $\mathcal{O}(1)$ deg², one week before merger with accurate chirp mass measurement with uncertainties $\mathcal{O}(10^{-5})$! The resulting sky areas are ideally suited for EM follow-up with wide-field telescopes enabling the discovery of short GRB afterglows, kilonovae, and other transient signatures with unprecedented temporal lead time. The improvement in sky-localization will facilitate stringent measurement of the Hubble constant [79].

Joint detections of compact binaries in the IndIGO-D and ground-based detectors also provide a powerful

framework for testing general relativity [80]. IndIGO-D would capture the early inspiral of a binary system over a large number of cycles, allowing for a precise determination of component masses and spins. Ground-based detectors would then probe the same systems during the late inspiral, merger, and ringdown, offering an independent measurement of the source's intrinsic parameters in a different dynamical regime. Comparing the low- and high-frequency inferences would enable stringent consistency tests of GR across widely separated frequency regimes [81, 82].

By filling the spectral gap between LISA and terrestrial detectors, IndIGO-D will enable practical multi-band observations possible where, many systems observable in the dHz regime will reappear in the high-frequency band within days or hours, rather than the decade-long delay characteristic of LISA-to-terrestrial detector transitions. This makes IndIGO-D uniquely suited for issuing timely early-warning alerts and enabling coordinated EM follow-up.

Appendix A: Effect of arm-length variation on round-trip laser phase shift

The overall antenna response of an interferometric GW detector is constructed from individual single-link Doppler measurements, which represent the fractional change in the frequency experienced by a laser beam as it propagates along the interferometer arm. We adopt the adiabatic approximation introduced in [83], and further used in [84] and [85] in the context of LISA, to model the antenna response of IndIGO-D. In this approach, the motion of the constellation is described as a sequence of stationary states. In each state, the detector is held motionless and the laser beam completes one round-trip across the detector's arms. This approximation holds when the timescale of frequency evolution of the chirping binary is longer compared to the light travel time between the arms.

The fractional change in the laser frequency induced by a GW, as it travels from the sending spacecraft s located at \vec{x}_s at barycenter time t_s and arrive at a receiving spacecraft r located at \vec{x}_r at barycenter time t_r is given by [86],

$$y_{sr}(t) = \frac{1}{2} \frac{\hat{l}^i(t) \hat{l}^j(t)}{1 - \hat{l}(t) \cdot \hat{k}} [h_{ij}(t_r, \vec{x}_r) - h_{ij}(t_s, \vec{x}_s)], \quad (\text{A1})$$

where, $\hat{l}(t)$ denotes the link unit vector from spacecraft s to r and is a time-dependent quantity due to the motion of the detector, $h_{ij}(t, \vec{x}) \equiv h_{ij}(t - \hat{k} \cdot \vec{x}/c, 0)$ is the metric perturbation describing a plane-parallel GW propagating

in the \hat{k} direction and is a linear combination of the two polarization states, e_{ij}^+ and e_{ij}^\times ,

$$h_{ij}(t, \vec{x}) = h_+(t, \vec{x}) e_{ij}^+ + h_\times(t, \vec{x}) e_{ij}^\times, \quad (\text{A2})$$

the basis polarization states of the GW are related to the reference polarization basis by,

$$\begin{pmatrix} e_{ij}^+ \\ e_{ij}^\times \end{pmatrix} = \begin{pmatrix} \cos 2\psi & \sin 2\psi \\ -\sin 2\psi & \cos 2\psi \end{pmatrix} \begin{pmatrix} \epsilon_{ij}^+ \\ \epsilon_{ij}^\times \end{pmatrix}, \quad (\text{A3})$$

where, ψ is the polarization angle that measures the angle by which the true polarization axes of GW are rotated with respect to the reference polarization axes.

Following [86], one can compute the fractional change in the laser frequency as it completes one round-trip across a single arm of the interferometer as a function of the GW frequency and is given by,

$$\tilde{\phi}(f; t) = 2\pi l \hat{l}^i \hat{l}^j e^{-2\pi i f \hat{k} \cdot \vec{x}_s / c} \tilde{h}_{ij}(f) \mathcal{T}(\hat{l} \cdot \hat{k}, f; t), \quad (\text{A4})$$

where,

$$\begin{aligned} \mathcal{T}(\hat{l} \cdot \hat{k}, f; t) := & \frac{1}{2} \left\{ e^{-i\pi f l (3 + \hat{k} \cdot \hat{l}) / c} \text{sinc} \left[\pi f l (1 - \hat{k} \cdot \hat{l}) / c \right] \right. \\ & \left. + e^{-i\pi f l (1 + \hat{k} \cdot \hat{l}) / c} \text{sinc} \left[\pi f l (1 + \hat{k} \cdot \hat{l}) / c \right] \right\}, \end{aligned} \quad (\text{A5})$$

is the transfer function. In Eqs. (A4) and (A5), the time dependence in the link unit vector, \hat{l} and arm-length, l is implicit and is not shown for brevity. In the frequency regime where $f l / c \ll 1$, the transfer function becomes a constant (unity) and this limit is regarded as the long wavelength limit (LWL). As evident from Fig. (2), there is a slight variation (a few ppm) in the lengths of the two interferometric arms during the motion of the constellation over a timescale of months. We would like to quantify the effect of this drift on the measured phase difference of the laser light in one round-trip across a single arm as given by Eq. (A4). Since the arm-length variation is small, we can write,

$$l(t) = l_0 [1 + \epsilon(t)], \quad \text{with } l_0 = 1000 \text{ km}, |\epsilon| \sim \mathcal{O}(10^{-6}). \quad (\text{A6})$$

We can Taylor expand $\tilde{\phi}(f, l; t)$ about $l = l_0$ to get,

$$\tilde{\phi}(f, l; t) = \tilde{\phi}_0(f, l_0; t) + \epsilon l_0 \left. \frac{\partial}{\partial l} \tilde{\phi}(f, l; t) \right|_{l=l_0} + \mathcal{O}(\epsilon^2), \quad (\text{A7})$$

where, $\tilde{\phi}_0(f, l_0; t)$ is the change in the phase of laser across one round-trip assuming static arm of length l_0 . Therefore, the fractional departure in the phase shift due to varying arm-length from the static case is,

$$\begin{aligned}
\frac{\delta\tilde{\phi}(f, l; t)}{\tilde{\phi}_0(f, l_0; t)} &= \epsilon \frac{l_0}{\tilde{\phi}_0} \frac{\partial}{\partial l} \tilde{\phi}(f, l; t) \Big|_{l=l_0}, \\
&= \epsilon \frac{l_0}{\tilde{\phi}_0} 2\pi f e^{-2\pi i f \hat{k} \cdot \vec{x}_s / c} \hat{l}^i \hat{l}^j \tilde{h}_{ij}(t) \left[\mathcal{T}(\hat{l} \cdot \hat{k}, f, l_0; t) + l_0 \frac{\partial}{\partial l} \mathcal{T}(\hat{l} \cdot \hat{k}, f, l; t) \Big|_{l=l_0} \right], \\
&= \epsilon \left[1 + \frac{x_0}{\tilde{\phi}_0(f, l_0; t)} 2\pi f e^{-2\pi i f \hat{k} \cdot \vec{x}_i / c} \hat{l}^i \hat{l}^j \tilde{h}_{ij}(t) \frac{\partial \mathcal{T}}{\partial x} \Big|_{x=x_0} \right], \tag{A8}
\end{aligned}$$

where, $x = \pi f l / c$. Note that the second term in the above expression does not even contribute for low frequencies where the transfer functions remain constant. The second term starts to contribute towards the higher end of the frequency spectrum, where the LWL approximation breaks down. Upon taking the derivative of the transfer function with respect to x and substituting in Eq. (A8), one can easily check that the dominant order contributions of the second term in Eq. (A8) are $\mathcal{O}(x_0^2)$ and $\mathcal{O}(x_0)$ corresponding to the real and imaginary parts, respectively.

In the bandwidth of interest for the dHz detector, i.e., $[0.01, 10]$ Hz, we have $x_0 \lesssim 0.1$. Thus, the fractional change is

$$\frac{\delta\tilde{\phi}(f, l; t)}{\tilde{\phi}_0(f, l_0; t)} \approx \epsilon = \mathcal{O}(10^{-6}). \tag{A9}$$

This implies that the contribution of the slowly drifting arms towards laser phase shift is suppressed by $\mathcal{O}(10^{-6})$ and are thus ignorable. This justifies the assumption of taking constant arm-lengths in Eq. (10).

Appendix B: Bayesian Parameter Estimation

Given the strain data $d(t)$ recorded by a detector network, containing a signal $h(\vec{\Lambda}_{\text{true}}; t)$ from a compact binary coalescence and additive noise $n(t)$, the aim of parameter estimation is to determine the posterior distribution $p(\vec{\Lambda} \mid d)$ for the source parameters. The posterior is related to the likelihood $p(d \mid \vec{\Lambda})$ and the prior $p(\vec{\Lambda})$ via Bayes' theorem:

$$p(\vec{\Lambda} \mid d) = \frac{p(d \mid \vec{\Lambda}) p(\vec{\Lambda})}{p(d)}, \tag{B1}$$

where $p(d)$ is the evidence, which acts as an overall normalization constant. For aligned-spin BNS systems, the parameter space is typically 13-dimensional, making direct evaluation of the posterior intractable. Stochastic sampling algorithms such as Markov chain Monte Carlo

(MCMC) [87] and nested sampling [88] are therefore employed to explore $p(\vec{\Lambda} \mid d)$. The binary parameters include a set of intrinsic source properties that govern the dynamics and phase evolution of the waveform (such as the component masses, spins and the tidal deformabilities) and a set of extrinsic parameters, namely, the source's sky location, polarization angle ψ , inclination angle ι , coalescence phase φ , coalescence time t_c in some preferred reference frame, and luminosity distance d_L . These extrinsic parameters affect the amplitude, arrival time, and modulation of the signal in the detectors.

For GW data $d^{(k)}(t) = h^{(k)}(\vec{\Lambda}_{\text{true}}; t) + n^{(k)}(t)$ recorded at the k^{th} detector, under the assumption of Gaussian and stationary noise $n^{(k)}(t)$, the phase-marginalized log-likelihood ratio of the signal hypothesis to the null hypothesis is given by

$$\ln \mathcal{L}(\vec{\Lambda}) = \ln I_0 \left| \sum_{k=1}^{N_d} \langle h^{(k)}(\vec{\Lambda}) \mid \mathbf{d}^{(k)} \rangle \right| - \frac{1}{2} \sum_{k=1}^{N_d} \left\| h^{(k)}(\vec{\Lambda}) \right\|^2, \tag{B2}$$

where, $I_0[\cdot]$ is the zeroth-order modified Bessel function of the first kind, N_d is the number of detectors in the network and $\langle a \mid b \rangle$ is the noise-weighted inner product of two time domain signal 'vectors' $a(t)$ and $b(t)$,

$$\langle a \mid b \rangle = 4 \Re \int_{f_{\min}}^{f_{\max}} \frac{\tilde{a}^*(f) \tilde{b}(f)}{S_n(f)} df, \tag{B3}$$

where, f_{\min} and f_{\max} are the lower and upper cut-off frequencies; $\|a\|^2 = \langle a \mid a \rangle$ denotes the norm and $\tilde{a}(f)$ denotes the Fourier transform of $a(t)$. In order to accelerate the sampling process, we adopt the heterodyning likelihood [71, 72] or the relative binning method [73] as implemented in the PyCBC Inference [89] library. We use the dynesty [90] nested sampling package as implemented in Bilby [91] with acceptance-walk sampling method, $n_{\text{live}} = 3000$ and $n_{\text{accept}} = 60$. The prior distributions for various parameters and their ranges used to obtain the results presented in Sec. IV E for various analyses with IndIGO-D are summarized in Table II. Note that the sky location is measured in the SSB

Parameters	Range	Prior distribution
\mathcal{M}	$[\mathcal{M}_{\text{inj}} \pm 10^{-3} \text{ M}_\odot] \propto \mathcal{M}$	
q	$[1, q_{\text{inj}} + 2]$	$\propto [(1+q)/q^3]^{2/5}$
$\chi_{1z, 2z}$	$[-0.05, 0.05]$	Uniform
d_L	$[1, 1000] \text{Mpc}$	Uniform in volume
t_c	$[t_c^{\text{inj}} \pm 60 \text{ s}]$	Uniform
λ	$[0, 2\pi]$	Uniform
β	$[-\pi/2, \pi/2]$	$\sin^{-1} [\text{Uniform}[-1, 1]]$
ι	$[0, \pi]$	Uniform in $\cos \iota$
ψ	$[0, 2\pi]$	Uniform
$\Lambda_{1,2}$	$[0, 5000]$	Uniform

TABLE II. The prior distributions over various parameters and their corresponding range used in the parameter estimation with IndIGO-D. The chosen prior distributions over \mathcal{M} and q correspond to uniform distributions over component masses. Priors over ecliptic longitude and latitude correspond to the isotropic direction across all sky.

frame in terms of ecliptic longitude and ecliptic latitude while sampling the posterior distribution, which are later transformed in the celestial coordinates.

ACKNOWLEDGMENTS

A. Sharma, D. Tahelyani and A. Sengupta gratefully acknowledge the hospitality of IUCAA, Pune, during our visits under the IUCAA Associates Program, where part of this research was conducted. We are grateful to the HPC facility at IIT Gandhinagar for access to computational resources, and especially to Raviraj Sukhadia for reliable support in maintaining the cluster. A. Sharma acknowledges IIT Gandhinagar for the senior research fellowship. D. Tahelyani acknowledges the support from the Inspire fellowship from the Department of Science and Technology of India, under fellowship number DST/INSPIRE Fellowship/[IF210643]. We thank our colleagues in the IndIGO consortium for suggestions and helpful discussions and providing the fiducial IndIGO-D noise curves.

We acknowledge the National Supercomputing Mission (NSM) for providing computing resources of ‘PARAM Ananta’ at IIT Gandhinagar, which is implemented by C-DAC and supported by the Ministry of Electronics and Information Technology (MeitY) and Dept. of Science and Technology (DST), Govt. of India.

[1] B. P. Abbott *et al.* (LIGO Scientific, Virgo), Observation of Gravitational Waves from a Binary Black Hole Merger, *Phys. Rev. Lett.* **116**, 061102 (2016), [arXiv:1602.03837 \[gr-qc\]](https://arxiv.org/abs/1602.03837).

[2] B. P. Abbott *et al.* (LIGO Scientific, Virgo), Properties of the Binary Black Hole Merger GW150914, *Phys. Rev. Lett.* **116**, 241102 (2016), [arXiv:1602.03840 \[gr-qc\]](https://arxiv.org/abs/1602.03840).

[3] B. Abbott *et al.* (The LIGO Scientific Collaboration, Virgo Collaboration), GWTC-1: A Gravitational-Wave Transient Catalog of Compact Binary Mergers Observed by LIGO and Virgo during the First and Second Observing Runs, *Physical Review X* **9**, 10.1103/physrevx.9.031040 (2019).

[4] R. Abbott *et al.* (The LIGO Scientific Collaboration, Virgo Collaboration), GWTC-2: Compact Binary Coalescences Observed by LIGO and Virgo during the First Half of the Third Observing Run, *Physical Review X* **11**, 10.1103/physrevx.11.021053 (2021).

[5] R. Abbott *et al.* (The LIGO Scientific Collaboration and the Virgo Collaboration), GWTC-2.1: Deep extended catalog of compact binary coalescences observed by LIGO and Virgo during the first half of the third observing run, *Phys. Rev. D* **109**, 022001 (2024).

[6] R. Abbott *et al.* (The LIGO Scientific Collaboration, Virgo Collaboration, and KAGRA Collaboration), GWTC-3: Compact Binary Coalescences Observed by LIGO and Virgo during the Second Part of the Third Observing Run, *Phys. Rev. X* **13**, 041039 (2023).

[7] A. G. Abac *et al.* (LIGO Scientific, VIRGO, KAGRA), GWTC-4.0: An Introduction to Version 4.0 of the Gravitational-Wave Transient Catalog, (2025), [arXiv:2508.18080 \[gr-qc\]](https://arxiv.org/abs/2508.18080).

[8] A. G. Abac *et al.* (LIGO Scientific, VIRGO, KAGRA), GWTC-4.0: Updating the Gravitational-Wave Transient Catalog with Observations from the First Part of the Fourth LIGO-Virgo-KAGRA Observing Run, (2025), [arXiv:2508.18082 \[gr-qc\]](https://arxiv.org/abs/2508.18082).

[9] B. P. Abbott *et al.* (The LIGO Scientific Collaboration and Virgo Collaboration), GW170817: Observation of Gravitational Waves from a Binary Neutron Star Inspiral, *Phys. Rev. Lett.* **119**, 161101 (2017).

[10] B. P. Abbott *et al.*, Multi-messenger Observations of a Binary Neutron Star Merger, *Astrophys. J. Lett.* **848**, L12 (2017), [arXiv:1710.05833 \[astro-ph.HE\]](https://arxiv.org/abs/1710.05833).

[11] B. P. Abbott *et al.* (LIGO Scientific, Virgo, 1M2H, Dark Energy Camera GW-E, DES, DLT40, Las Cumbres Observatory, VINROUGE, MASTER), A gravitational-wave standard siren measurement of the Hubble constant, *Nature* **551**, 85 (2017), [arXiv:1710.05835 \[astro-ph.CO\]](https://arxiv.org/abs/1710.05835).

[12] D. Kasen, B. Metzger, J. Barnes, E. Quataert, and E. Ramirez-Ruiz, Origin of the heavy elements in binary

neutron-star mergers from a gravitational wave event, *Nature* **551**, 80 (2017), arXiv:1710.05463 [astro-ph.HE].

[13] B. P. Abbott *et al.* (LIGO Scientific, Virgo, Fermi-GBM, INTEGRAL), Gravitational Waves and Gamma-rays from a Binary Neutron Star Merger: GW170817 and GRB 170817A, *Astrophys. J. Lett.* **848**, L13 (2017), arXiv:1710.05834 [astro-ph.HE].

[14] A. G. Abac *et al.* (LIGO Scientific, VIRGO, KAGRA), GWTC-4.0: Population Properties of Merging Compact Binaries, (2025), arXiv:2508.18083 [astro-ph.HE].

[15] J. Aasi *et al.* (LIGO Scientific), Advanced LIGO, *Class. Quant. Grav.* **32**, 074001 (2015), arXiv:1411.4547 [gr-qc].

[16] P. Amaro-Seoane *et al.* (LISA), Laser Interferometer Space Antenna, (2017), arXiv:1702.00786 [astro-ph.IM].

[17] I. Mandel, A. Sesana, and A. Vecchio, The astrophysical science case for a decihertz gravitational-wave detector, *Class. Quant. Grav.* **35**, 054004 (2018), arXiv:1710.11187 [astro-ph.HE].

[18] K. A. Kuns, H. Yu, Y. Chen, and R. X. Adhikari, Astrophysics and cosmology with a decihertz gravitational-wave detector: TianGO, *Phys. Rev. D* **102**, 043001 (2020), arXiv:1908.06004 [gr-qc].

[19] M. A. Sedda *et al.*, The missing link in gravitational-wave astronomy: discoveries waiting in the decihertz range, *Class. Quant. Grav.* **37**, 215011 (2020), arXiv:1908.11375 [gr-qc].

[20] IndIGO – Indian Initiative in Gravitational-wave Observations, <https://www.gw-indigo.org> (2025), accessed: 2025-12-23.

[21] IndIGO-D Collaboration, Science Cases and Mission Concept for a Michelson-like Deci-Hertz Space-Based Gravitational-Wave Observatory (2026), manuscript in preparation.

[22] S. Kawamura *et al.*, The Japanese space gravitational wave antenna DECIGO, *Class. Quant. Grav.* **23**, S125 (2006).

[23] S. Sato *et al.*, The status of DECIGO, *J. Phys. Conf. Ser.* **840**, 012010 (2017).

[24] S. Kawamura *et al.*, Current status of space gravitational wave antenna DECIGO and B-DECIGO, *PTEP* **2021**, 05A105 (2021), arXiv:2006.13545 [gr-qc].

[25] J. Harms *et al.* (LGWA), Lunar Gravitational-wave Antenna, *Astrophys. J.* **910**, 1 (2021), arXiv:2010.13726 [gr-qc].

[26] P. Ajith *et al.*, The Lunar Gravitational-wave Antenna: mission studies and science case, *JCAP* **01**, 108, arXiv:2404.09181 [gr-qc].

[27] A. B. Yelikar and K. Jani, Binary Neutron Stars from the Moon: Early Warnings and Precision Science for the Artemis Era, (2025), arXiv:2510.05400 [gr-qc].

[28] K. Jani *et al.*, Laser Interferometer Lunar Antenna (LILA): Advancing the U.S. Priorities in Gravitational-wave and Lunar Science, (2025), arXiv:2508.11631 [gr-qc].

[29] T. Creighton, P. Lognonné, M. P. Panning, J. Trippe, V. Quetschke, and K. Jani, Fundamental Noise and Gravitational-Wave Sensitivity of the Laser Interferometer Lunar Antenna (LILA), (2025), arXiv:2508.18437 [gr-qc].

[30] S. V. Dhurandhar, K. Rajesh Nayak, S. Koshti, and J. Y. Vinet, Fundamentals of the LISA stable flight formation, *Class. Quant. Grav.* **22**, 481 (2005), arXiv:gr-qc/0410093.

[31] L. Sun, E. Goetz, J. S. Kissel, *et al.*, Characterization of systematic error in Advanced LIGO calibration, *Classical and Quantum Gravity* **37**, 225008 (2020).

[32] R. Gamba, M. Breschi, S. Bernuzzi, M. Agathos, and A. Nagar, Waveform systematics in the gravitational-wave inference of tidal parameters and equation of state from binary neutron-star signals, *Phys. Rev. D* **103**, 124015 (2021).

[33] E. Savalle, J. Gair, L. Speri, and S. Babak, Assessing the impact of instrumental calibration uncertainty on lisa science, *Phys. Rev. D* **106**, 022003 (2022).

[34] R. X. Adhikari, N. Smith, A. Brooks, L. Barsotti, B. Shapiro, B. Lantz, D. McClelland, E. K. Gustafson, D. V. Martynov, V. Mitrofanov, D. Coyne, K. Arai, C. Torrie, and C. Wipf, *LIGO Voyager Upgrade: Design Concept*, Technical Report No. LIGO-T1400226 (2018).

[35] IndIGO-D Collaboration, IndIGO: Decihertz gravitational-wave observatory repository, <https://gitlab.com/rajesh.nayak/indigo> (2024), accessed: 2026-01-06.

[36] S. Khan, S. Husa, M. Hannam, F. Ohme, M. Pürer, X. Jiménez Forteza, and A. Bohé, Frequency-domain gravitational waves from nonprecessing black-hole binaries. II. A phenomenological model for the advanced detector era, *Phys. Rev. D* **93**, 044007 (2016), arXiv:1508.07253 [gr-qc].

[37] N. Aghanim *et al.* (Planck), Planck 2018 results. VI. Cosmological parameters, *Astron. Astrophys.* **641**, A6 (2020), [Erratum: Astron. Astrophys. 652, C4 (2021)], arXiv:1807.06209 [astro-ph.CO].

[38] D. Shoemaker (LIGO Scientific), Gravitational wave astronomy with LIGO and similar detectors in the next decade, (2019), arXiv:1904.03187 [gr-qc].

[39] A. Sesana, J. Gair, I. Mandel, and A. Vecchio, Observing gravitational waves from the first generation of black holes, *Astrophys. J. Lett.* **698**, L129 (2009), arXiv:0903.4177 [astro-ph.CO].

[40] J. Bellovary, A. Brooks, M. Colpi, M. Eracleous, K. Holley-Bockelmann, A. Hornschemeier, L. Mayer, P. Natarajan, J. Slutsky, and M. Tremmel, Where are the Intermediate Mass Black Holes?, (2019), arXiv:1903.08144 [astro-ph.HE].

[41] P. Gondolo and J. Silk, Dark matter annihilation at the galactic center, *Phys. Rev. Lett.* **83**, 1719 (1999), arXiv:astro-ph/9906391.

[42] P. Ullio, H. Zhao, and M. Kamionkowski, A Dark matter spike at the galactic center?, *Phys. Rev. D* **64**, 043504 (2001), arXiv:astro-ph/0101481.

[43] L. Sadeghian, F. Ferrer, and C. M. Will, Dark matter distributions around massive black holes: A general relativistic analysis, *Phys. Rev. D* **88**, 063522 (2013),

arXiv:1305.2619 [astro-ph.GA].

[44] A. M. Green and B. J. Kavanagh, Primordial Black Holes as a dark matter candidate, *J. Phys. G* **48**, 043001 (2021), arXiv:2007.10722 [astro-ph.CO].

[45] M. Boudaud, T. Lacroix, M. Stref, J. Lavalle, and P. Salati, In-depth analysis of the clustering of dark matter particles around primordial black holes. Part I. Density profiles, *JCAP* **08**, 053, arXiv:2106.07480 [astro-ph.CO].

[46] E. Barausse, V. Cardoso, and P. Pani, Can environmental effects spoil precision gravitational-wave astrophysics?, *Phys. Rev. D* **89**, 104059 (2014), arXiv:1404.7149 [gr-qc].

[47] K. Eda, Y. Itoh, S. Kuroyanagi, and J. Silk, New Probe of Dark-Matter Properties: Gravitational Waves from an Intermediate-Mass Black Hole Embedded in a Dark-Matter Minispike, *Phys. Rev. Lett.* **110**, 221101 (2013), arXiv:1301.5971 [gr-qc].

[48] K. Eda, Y. Itoh, S. Kuroyanagi, and J. Silk, Gravitational waves as a probe of dark matter minispikes, *Phys. Rev. D* **91**, 044045 (2015), arXiv:1408.3534 [gr-qc].

[49] C. F. B. Macedo, P. Pani, V. Cardoso, and L. C. B. Crispino, Into the lair: gravitational-wave signatures of dark matter, *Astrophys. J.* **774**, 48 (2013), arXiv:1302.2646 [gr-qc].

[50] B. J. Kavanagh, D. A. Nichols, G. Bertone, and D. Gaggero, Detecting dark matter around black holes with gravitational waves: Effects of dark-matter dynamics on the gravitational waveform, *Phys. Rev. D* **102**, 083006 (2020), arXiv:2002.12811 [gr-qc].

[51] A. Coogan, G. Bertone, D. Gaggero, B. J. Kavanagh, and D. A. Nichols, Measuring the dark matter environments of black hole binaries with gravitational waves, *Phys. Rev. D* **105**, 043009 (2022), arXiv:2108.04154 [gr-qc].

[52] A. M. Derdzinski, D. D’Orazio, P. Duffell, Z. Haiman, and A. MacFadyen, Probing gas disc physics with LISA: simulations of an intermediate mass ratio inspiral in an accretion disc, *Mon. Not. Roy. Astron. Soc.* **486**, 2754 (2019), [Erratum: Mon. Not. Roy. Astron. Soc. 489, 4860–4861 (2019)], arXiv:1810.03623 [astro-ph.HE].

[53] B. Kocsis, N. Yunes, and A. Loeb, Observable Signatures of EMRI Black Hole Binaries Embedded in Thin Accretion Disks, *Phys. Rev. D* **84**, 024032 (2011), arXiv:1104.2322 [astro-ph.GA].

[54] D. Tahelyani, A. Bhattacharyya, and A. S. Sengupta, Probing dark matter halo profiles with multiband observations of gravitational waves, *Phys. Rev. D* **111**, 083041 (2025), arXiv:2411.14063 [gr-qc].

[55] X. Chen and P. Amaro-Seoane, Revealing the formation of stellar-mass black hole binaries: The need for deci-Hertz gravitational wave observatories, *Astrophys. J. Lett.* **842**, L2 (2017), arXiv:1702.08479 [astro-ph.HE].

[56] R. M. O’Leary, B. Kocsis, and A. Loeb, Gravitational waves from scattering of stellar-mass black holes in galactic nuclei, *Mon. Not. Roy. Astron. Soc.* **395**, 2127 (2009), arXiv:0807.2638 [astro-ph].

[57] P. C. Peters and J. Mathews, Gravitational radiation from point masses in a Keplerian orbit, *Phys. Rev.* **131**, 435 (1963).

[58] F. Antonini and H. B. Perets, Secular evolution of compact binaries near massive black holes: Gravitational wave sources and other exotica, *Astrophys. J.* **757**, 27 (2012), arXiv:1203.2938 [astro-ph.GA].

[59] J. Samsing, M. MacLeod, and E. Ramirez-Ruiz, The Formation of Eccentric Compact Binary Inspirals and the Role of Gravitational Wave Emission in Binary-Single Stellar Encounters, *Astrophys. J.* **784**, 71 (2014), arXiv:1308.2964 [astro-ph.HE].

[60] W. E. East, S. T. McWilliams, J. Levin, and F. Pretorius, Observing complete gravitational wave signals from dynamical capture binaries, *Phys. Rev. D* **87**, 043004 (2013), arXiv:1212.0837 [gr-qc].

[61] H. Ziaeepour, Binary Neutron Star (BNS) Merger: What We Learned from Relativistic Ejecta of GW/GRB 170817A, *MDPI Physics* **1**, 194 (2019), arXiv:1905.11355 [astro-ph.HE].

[62] J.-S. Wang, F.-K. Peng, K. Wu, and Z.-G. Dai, Pre-merger electromagnetic counterparts of binary compact stars, *Astrophys. J.* **868**, 19 (2018), arXiv:1810.00170 [astro-ph.HE].

[63] B. Crinquant, B. Cerutti, and G. Dubus, Kinetic modeling of the electromagnetic precursor from an axisymmetric binary pulsar coalescence, *Astron. Astrophys.* **622**, A161 (2019), arXiv:1812.05898 [astro-ph.HE].

[64] E. R. Most and A. A. Philippov, Electromagnetic precursors to gravitational wave events: Numerical simulations of flaring in pre-merger binary neutron star magnetospheres, *Astrophys. J. Lett.* **893**, L6 (2020), arXiv:2001.06037 [astro-ph.HE].

[65] N. Sridhar, J. Zrake, B. D. Metzger, L. Sironi, and D. Giannios, Shock-powered radio precursors of neutron star mergers from accelerating relativistic binary winds, *Mon. Not. Roy. Astron. Soc.* **501**, 3184 (2021), arXiv:2010.09214 [astro-ph.HE].

[66] E. R. Most and A. A. Philippov, Electromagnetic precursor flares from the late inspiral of neutron star binaries, *Mon. Not. Roy. Astron. Soc.* **515**, 2710 (2022), arXiv:2205.09643 [astro-ph.HE].

[67] K. P. Mooley, A. T. Deller, O. Gottlieb, E. Nakar, G. Hallinan, S. Bourke, D. A. Frail, A. Horesh, A. Corsi, and K. Hotokezaka, Superluminal motion of a relativistic jet in the neutron-star merger GW170817, *Nature* **561**, 355 (2018), arXiv:1806.09693 [astro-ph.HE].

[68] T. Dietrich *et al.*, Matter imprints in waveform models for neutron star binaries: Tidal and self-spin effects, *Phys. Rev. D* **99**, 024029 (2019), arXiv:1804.02235 [gr-qc].

[69] T. Dietrich, A. Samajdar, S. Khan, N. K. Johnson-McDaniel, R. Dudi, and W. Tichy, Improving the NRTidal model for binary neutron star systems, *Phys. Rev. D* **100**, 044003 (2019), arXiv:1905.06011 [gr-qc].

[70] I. M. Romero-Shaw *et al.*, Bayesian inference for compact binary coalescences with BILBY: validation and

application to the first LIGO–Virgo gravitational-wave transient catalogue, *Mon. Not. Roy. Astron. Soc.* **499**, 3295 (2020), arXiv:2006.00714 [astro-ph.IM].

[71] N. J. Cornish, Fast Fisher Matrices and Lazy Likelihoods, arXiv preprint (2010), arXiv:1007.4820 [gr-qc].

[72] N. J. Cornish, Heterodyned likelihood for rapid gravitational wave parameter inference, *Phys. Rev. D* **104**, 104054 (2021), arXiv:2109.02728 [gr-qc].

[73] B. Zackay, L. Dai, and T. Venumadhav, Relative Binning and Fast Likelihood Evaluation for Gravitational Wave Parameter Estimation, arXiv preprint (2018), arXiv:1806.08792 [astro-ph.IM].

[74] S. Nissanke, M. Kasliwal, and A. Georgieva, Identifying elusive electromagnetic counterparts to gravitational wave mergers: an end-to-end simulation, *The Astrophysical Journal* **767**, 124 (2013), arXiv:1210.6362 [astro-ph.CO].

[75] W. B. Atwood *et al.* (Fermi-LAT), The Large Area Telescope on the Fermi Gamma-ray Space Telescope Mission, *Astrophys. J.* **697**, 1071 (2009), arXiv:0902.1089 [astro-ph.IM].

[76] Ž. Ivezić, S. M. Kahn, J. A. Tyson, B. Abel, E. Acosta, R. Allsman, D. Alonso, Y. AlSayyad, S. F. Anderson, J. Andrew, *et al.*, LSST: From science drivers to reference design and anticipated data products, *Astrophysical Journal* **873**, 111 (2019), arXiv:0805.2366.

[77] S. Valenti, D. J. Sand, S. Yang, E. Cappellaro, L. Tartaglia, A. Corsi, S. W. Jha, D. E. Reichart, J. Haislip, and V. Kouprianov, The discovery of the electromagnetic counterpart of GW170817: Kilonova AT 2017gfo/DLT17ck, *The Astrophysical Journal Letters* **848**, L24 (2017), arXiv:1710.05854 [astro-ph.HE].

[78] B. Margalit and B. D. Metzger, The Multi-Messenger Matrix: the Future of Neutron Star Merger Constraints on the Nuclear Equation of State, *Astrophys. J. Lett.* **880**, L15 (2019), arXiv:1904.11995 [astro-ph.HE].

[79] B. C. Seymour, H. Yu, and Y. Chen, Multiband gravitational wave cosmography with dark sirens, *Phys. Rev. D* **108**, 044038 (2023), arXiv:2208.01668 [gr-qc].

[80] A. Sesana, Prospects for Multiband Gravitational-Wave Astronomy after GW150914, *Phys. Rev. Lett.* **116**, 231102 (2016), arXiv:1602.06951 [gr-qc].

[81] A. Ghosh *et al.*, Testing general relativity using golden black-hole binaries, *Phys. Rev. D* **94**, 021101 (2016), arXiv:1602.02453 [gr-qc].

[82] E. Barausse, N. Yunes, and K. Chamberlain, Theory-Agnostic Constraints on Black-Hole Dipole Radiation with Multiband Gravitational-Wave Astrophysics, *Phys. Rev. Lett.* **116**, 241104 (2016), arXiv:1603.04075 [gr-qc].

[83] L. J. Rubbo, N. J. Cornish, and O. Poujade, Forward modeling of space borne gravitational wave detectors, *Phys. Rev. D* **69**, 082003 (2004), arXiv:gr-qc/0311069.

[84] N. J. Cornish and K. Shuman, Black Hole Hunting with LISA, *Phys. Rev. D* **101**, 124008 (2020), arXiv:2005.03610 [gr-qc].

[85] A. Sharma, A. S. Sengupta, and S. Mukherjee, Accelerated parameter estimation of supermassive black hole binaries in LISA using a meshfree approximation, *Phys. Rev. D* **111**, 042009 (2025), arXiv:2409.14288 [gr-qc].

[86] J. D. E. Creighton and W. G. Anderson, *Gravitational-Wave Physics and Astronomy: An Introduction to Theory, Experiment and Data Analysis* (Wiley-VCH, Weinheim, 2011).

[87] D. Foreman-Mackey, D. W. Hogg, D. Lang, and J. Goodman, emcee: The MCMC Hammer, *Publ. Astron. Soc. Pac.* **125**, 306 (2013).

[88] J. Skilling, Nested sampling for general Bayesian computation, *Bayesian Anal.* **1**, 833 (2006).

[89] C. M. Biwer, C. D. Capano, S. De, M. Cabero, D. A. Brown, A. H. Nitz, and V. Raymond, PyCBC Inference: A Python-based parameter estimation toolkit for compact binary coalescence signals, *Publ. Astron. Soc. Pac.* **131**, 024503 (2019), arXiv:1807.10312 [astro-ph.IM].

[90] J. S. Speagle, dynesty: a dynamic nested sampling package for estimating Bayesian posteriors and evidences, *Mon. Not. Roy. Astron. Soc.* **493**, 3132 (2020), arXiv:1904.02180 [astro-ph.IM].

[91] G. Ashton *et al.*, BILBY: A user-friendly Bayesian inference library for gravitational-wave astronomy, *Astrophys. J. Suppl.* **241**, 27 (2019), arXiv:1811.02042 [astro-ph.IM].